Nanoscale

Accepted Manuscript

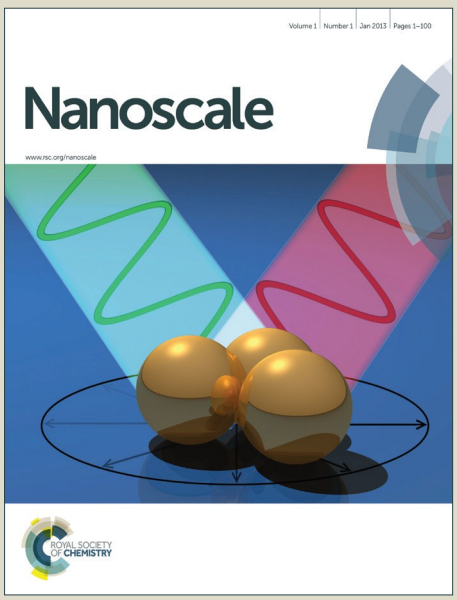

ROYAL SOCIETY OF CHEMISTRY

www.rsc.org/nanoscale

Functionalized ZnO@TiO_2 nanorod array film loaded with $ZnIn_{0.25}Cu_{0.02}S_{1.395}$ solid-solution: synthesis, characterization and enhanced visible light driven water splitting†

Ruosong Wang,[a] Xiaoxue Xu, [c] Yi Zhang,[a] Zhimin Chang,[a] Zaicheng Sun,[b*] and Wen-Fei Dong [a*]

[a] *CAS Key Laboratory of Bio-Medical Diagnostics, Suzhou Institute of Biomedical Engineering and Technology, Chinese Academy of Science (CAS), 88 Keling Road, Suzhou 215163, People's Republic of China.* [*]*E-mail: wenfeidong@126.com*

[b]*Beijing Key Laboratory for Green Catalysis and Separation, Department of Chemistry and Chemical Engineering, Beijing University of Technology, Beijing 100124, People's Republic of China.* [*]*E-mail: sunzc@ciomp.ac.cn*

[c] *Advanced Cytometry Labs, ARC Centre of Excellence for Nanoscale BioPhotonics(CNBP), Macquarie University, Sydney, NSW, 2109, Australia.*

† Electronic supplementary information (ESI) available: More SEM and TEM images, XRD patterns, EDX spectra and hydrogen production data.

Abstract

We design a novel semiconductor core/layer nanostructure of the uniform ZnO@TiO_2 nanorod array modified with $ZnIn_{0.25}Cu_{0.02}S_{1.395}$ solid-solution on the surface via a facile hydrothermal synthesis. This novel nanostructure combines the merits of all components and meets the requirements of photovoltaic systems application. An intimate PN heterojunction is formed from the ZnO@TiO_2 nanorod and polymetallic sulphide solid-solution, which is remarkably beneficial for the effective visible light absorption and rapid charge carrier separation. The nanostructures exhibit higher photocurrent and incident photon to electron conversion efficiency (IPCE) under no bias potential versus the Ag/AgCl electrode. We also analyzed the interface and photoelectrochemical characteristics of the nanostructure and revealed the kinetic process of the electron and hole transmission. In addition, the photoanode test shows the hydrogen production capability of the nanostructures from solar water splitting. These results verified that the ZnO and TiO_2 can be sensitized by the polymetallic sulfide for UV-Vis light driven energy conversion. Importantly, the approach we used to design the photoanode enables the development of the micro-nanoelectronic devices with enhanced performance.

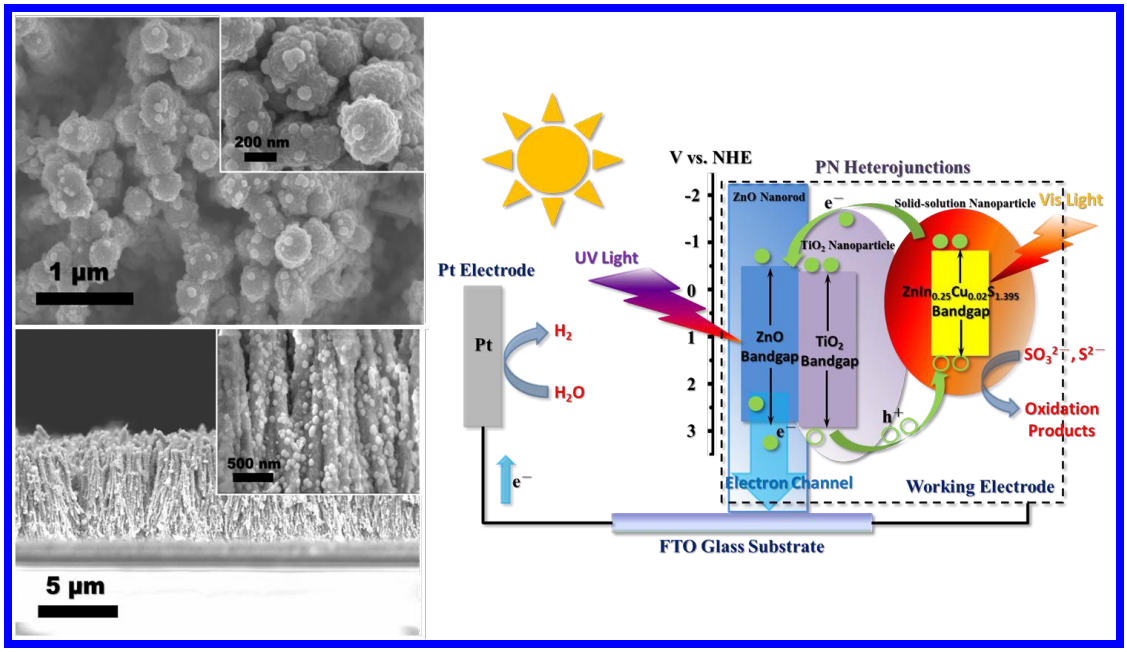

Keywords

hydrothermal synthesis, ZnO@TiO_2 nanorod, metallic sulphide solid-solution, visible light driven, photoelectric properties

Introduction

Due to the growing global energy demand and the increasing concerns on the energy-related environmental problems, solar energy, a sustainable and clean energy, has been considered as a potential energy source to tackle the energy and environmental issues.[1-8] Therefore, great efforts have been contributed to convert sunlight into usable energy effectively and economically. Photoelectrochemical (PEC) water splitting using solar illumination is proposed for the production of hydrogen fuel, because it is a simple and green process with high energy density.[9-12] Highly efficient and stable PEC systems have been employed for water splitting based on semiconducting materials, including TiO_2, Fe_2O_3, and ZnO.[13-18] Among them, ZnO single-crystal nanorod array is one of the excellent candidates as the photoelectrodes due to its great electron percolation pathways and light-harvesting ability.[19-21] On the other hand, anatase TiO_2 nanocrystals exposing the active facets [22-24] can be used to modify the surface of the individual ZnO single-crystal nanorod to improve the chemical stability of ZnO nanorod in acidic or basic environment. More importantly, the surface modification of ZnO nanorod using TiO_2 nanocrystals can also enhance the surface activity via the compatible crystal lattice parameters and band gap between ZnO and TiO_2.

However, both ZnO and TiO_2 are wide band gap semiconductors and they are only sensitive to UV light and exhibit fast recombination of the exciton which results in lower conversion efficiency of solar energy.[25-27] The metallic sulphide semiconductors with narrow band gap have recently been employed to decorate the

surface of ZnO nanowires for the extended visible light absorption, such as CdS, CdSe, and PbS. [28-34] The heterojunction interfaces of the oxides (TiO_2 or ZnO) and metallic sulphides can facilitate the separation and transportation of photogenerated charge carriers and thus improve the kinetics of water splitting processes to extend the lifetime of the charge.[27, 35-37] However, the toxicity of Cd, Se, and Pb elements in the metallic sulphides is still a big concern. In addition, CdS quantum dots, possessing relatively slower interfacial hole transfer rate compared to electron injection into metal oxides, cause hole-induced anodic corrosion.[38, 39]

In this work, we proposed a new polymetallic sulphide solid-solution to decorate the hierarchical nanostructure of the co-axial ZnO@TiO_2 nanorod array as the photoelectrode for the solar driven PEC device. We characterized sample morphology, crystal phase and elements. The optical absorption properties and interface properties were also analyzed. The mechanism of electron transmission kinetics of the novel hierarchical nanostructure was investigated. In addition, we performed the photoelectrochemical tests for the photovoltaic applications. We concluded that the novel hierarchical nanostructure of the co-axial ZnO@TiO_2 nanorod array decorated with polymetallic sulphide solid-solution is a promising multifunctional nanomaterial candidate for the micro/nano photoelectronic systems of biological sensing and medical detection.[40-42]

Results and discussion

The fabrication procedure of the hierarchical nanostructure of the co-axial ZnO@TiO_2 nanorod array decorated with the polymetallic sulfide solid-solution via hydrothermal synthesis is illustrated in Scheme 1. The fluorine-doped tin oxide (FTO) glass substrate spin-coated with ZnO seeds was put into the growth solution to get the ZnO nanorod array (ZnO NRA). Then TiO_2 was coated outside of each ZnO nanorod to form ZnO@TiO_2 nanorod array (ZnO@TiO_2 NRA). Finally, a variety of nanorod array samples loaded different amount of polymetallic sulfide solid-solution on the surface were obtained. They were named as from ZICS-1unit to ZICS-20unit according to the stoichiometry defined by the amount and concentration of the reaction mixture (see Experimental Section).

Morphology, structure and composition analysis

Figure 1 shows the typical top-view and side-view of the ZnO NRA, ZnO@TiO_2 NRA and ZICS-15unit grown on FTO substrates using field emission scanning electron microscope (FESEM). It can be seen from Figure 1A and D that ZnO nanorods with diameter of about 180 nm are perpendicularly aligned on the FTO substrate. The ZnO nanorod is in the shape of hexagonal prism with even lateral surfaces. Due to fast axial direction growth, the top of ZnO nanorod is sharp (inset in Figure 1A). Figure 1B and C show the top-view images of ZnO@TiO_2 NRA and ZICS-15unit, respectively. It can be seen that the surface of ZnO@TiO_2 nanorod becomes rough and a nanostructured layer consisting of many unordered nanoparticles is formed. Some bright sphere nanoparticles and aggregates are

irregularly distributed on the top and lateral surfaces of ZICS-15unit. The nanorod diameters of ZnO@TiO_2 NRA and ZICS-15unit increase to about 200 nm. From the corresponding side-view images (Figure 1E and F), it is also clearly shown that the TiO_2 nanoparticle layer wraps the ZnO nanorod, and the nanoparticles and aggregates are decorated onto the surface of nanorod. The length of each ZnO nanorod is about 7 μm, and it is barely changed with the coating of TiO_2 and sulfides. The energy-dispersive X-ray spectroscopy (EDX) analysis show that Zn and O, Zn, Ti and O, and Zn, Ti, Cu, In and S element co-exist in the ZnO NRA, ZnO@TiO_2 NRA and ZICS-15unit samples, respectively (see Figure S1 in supporting information).

Figure 1G～I show the X-ray diffraction (XRD) patterns of the ZnO NRA, ZnO@TiO_2 NRA and ZICS-15unit, respectively. The crystal structure of the ZICS powder, which is centrifugally collected from ZICS-15unit reaction liquid, is used as reference (inset of Figure 1I). A pronounced (002) diffraction peak of ZnO is shown in Figure 1 due to the highly oriented ZnO nanorod array. The diffraction peak from other directions is relatively weak. It is hard to observe diffraction peaks of TiO_2 due to the small amount of TiO_2 on the ZnO nanorod surfaces. Trace amount ZnS diffraction peaks is observed from the ZICS-15unit sample. This could be probably attributed to the penetration of the sulfide through the TiO_2 layer and reaction with the ZnO nanorod in the hydrothermal environment. The XRD pattern of ZICS powder shows three broad peaks corresponding to (111), (220), and (311) of $ZnIn_{0.25}Cu_{0.02}S_{1.395}$, respectively.[43] With the increase amount of sulfide, ZICS-20unit sample shows stronger ZnS diffraction peaks (see Figure S2 in

supporting information), which agrees well with the lattice spacing of ZnS nanoparticles observed in high resolution transmission electron microscopy (TEM) images of ZICS-20unit sample (see Figure S4 in supporting information). Based on above results, we can conclude that the $ZnIn_{0.25}Cu_{0.02}S_{1.395}$ aggregates were successfully decorated onto the surfaces of the co-axial ZnO@TiO_2 nanorod array.

High resolution transmission electron microscopy (HRTEM) images and element mapping of the ZICS-15unit sample results are shown in Figure 2. Figure 2A reveals that the outside of the ZnO@TiO_2 nanorod consists of randomly-oriented hemisphere nanoparticles and aggregates with the size of 15～50 nm. The magnification of selected partial nanorod area (Figure 2B) reveals a layer of TiO_2 nanoparticles about 10 nm thick wrapping the surface of ZnO nanorod. From Figure 2C, the inner ZnO nanorod with unitary lattice fringes is a characteristic sign of single-crystal structure, and the fringe spacing of 0.26 nm corresponds to the (002) plane of wurtzite type ZnO, which agree with the XRD patterns of related samples shown in Figure 1. We can also find that the nanoparticle layer from the surface to the inside has a polycrystalline structure, and crystal grains have the fringe spacings of 0.19 nm and 0.31 nm, which match well with the interplanar spacings of the (002) plane of TiO_2 and the (111) plane of $ZnIn_{0.25}Cu_{0.02}S_{1.395}$, respectively.[18, 22-24, 43] Moreover, it is further verified that $ZnIn_{0.25}Cu_{0.02}S_{1.395}$ forms solid-solution rather than compound mixture of ZnS, In_2S_3 and CuS due to its unitary fringe spacing and characteristic diffraction peak. Figure 2D shows the line scan profile of the EDX spectra acquired along a line crossing the nanorod as shown in the inset (high angle annular dark-field scanning

TEM (HAADF-STEM) image). The intensity of the curves provides evidence of the distribution density of all the elements indicating the core/layer structure. To confirm the multiple layer structure, element distribution mapping results are shown in Figure 2E. The left STEM image shows the nanorod decorated with sulfide aggregates. The Zn element is well dispersed in whole nanorod and aggregates due to both nanorod and aggregates contain Zn. In the Ti-k image, only the two edges of the nanorod show maxima, indicating that Ti only exists in the outer layer around the ZnO nanorod. On the contrary, the O element locates on the position of the nanorod because O mainly contributes from ZnO and TiO_2. On the aggregates, the O element signal obviously turns darker than that of the nanorod. Most of the S element locates on the aggregate site. These results clearly indicate that TiO_2 nanoparticle layer well wraps the ZnO nanorod, and polymetallic sulfide solid-solution forms nanoparticles and aggregates mingled onto the surface.

Absorption characterization

The optical absorption properties of the samples were tested. The UV-Vis absorption spectra and optical images of a series of nanorod array films on the FTO substrates are shown in Figure 3. ZnO NRA and ZnO@TiO_2 NRA are white and show no absorption in the visible light range. Their absorption edges are below 400 nm in the UV light region. After loaded $ZnIn_{0.25}Cu_{0.02}S_{1.395}$ solid-solution, the nanorod array sample displayed colors from light yellow to dark brown with the increased amount of sulfide. The corresponding band edges of absorption spectra red-shift from 521 nm to 582 nm in visible light region, that is to say, the corresponding bandgap varies from

2.39 eV to 2.14 eV by adjusting the loading amount of $ZnIn_{0.25}Cu_{0.02}S_{1.395}$ solid-solution while the absorption intensity also increases. However, an obvious absorption peak is observed in the UV-Vis spectrum of the ZICS-20unit sample, and the peak is probable due to the intensive scattering of small nanoparticles by loading excess $ZnIn_{0.25}Cu_{0.02}S_{1.395}$ solid-solution. In sum, it demonstrates that loading $ZnIn_{0.25}Cu_{0.02}S_{1.395}$ solid-solution onto the co-axial ZnO@TiO_2 nanorod array enhances the absorption coefficiency within a larger proportion of visible light to generate more photoinduced charge carriers.

Photoluminescence characterization

The photoluminescence spectra are shown in Figure 4, and the kinetic mechanism of electron transmission and material interface properties of our samples was investigated. For 220 nm laser excitation (Figure 4A), a ZnO intrinsic emission peak is at 400 nm, which increases with the loading amount of the sulphide. However, an intensity decrease was observed for the ZICS-20unit sample at 400 nm. It is probably because of the corrosion of the ZnO nanorod from over loading of sulphide (see Figure S3 in supporting information). The peaks located around 420 nm and 470 nm are attributed to the deep energy states caused by impurities of the ZnO nanorod, the broad spectra around 450 nm are assigned to the TiO_2 nanoparticle shell, and the broad baselines from 475 nm to 600 nm in visible light region are brought about by loading polymetallic sulphide solid-solution. The ZICS powder has no evident emission peaks in this region under the same excitation. Furthermore, when 450 nm laser excitation was applied (Figure 4B), the peak around 550 nm of the ZICS powder,

intrinsic emission of polymetallic sulphide solid-solution, gradually disappeared with sulphide addition. According to the comparison of different laser excitations, we can infer that the existence of electron transfer between core/layer interfaces under solar UV-Vis light illumination. First, both the inner ZnO nanorod and the outer layer including TiO_2 and polymetallic sulfide solid-solution are excited by UV light, so the electron transfer from sulphide to ZnO leads to strengthen the intrinsic emission of ZnO. Second, only the $ZnIn_{0.25}Cu_{0.02}S_{1.395}$ solid-solution can absorb the visible light and rapidly carry the excited electrons to ZnO through the stepwise energy level arrangements. Then the inner ZnO nanorod acts as good electron transport channel to achieve fast separation of photoinduced electrons and holes in working circuits.

Photoelectrochemical measurements

Figure 5A shows the *J-V* characteristics and current-time transient responses of these samples to evaluate their photoelectrochemical activity. Linear sweep voltammograms (LSV) are operated both in dark and under visible light irradiation. In the dark, all electrodes show tiny currents without any difference. Therefore, only the current curve of the ZnO NRA electrode is illustrated in dash line in Figure 5A. Under visible light illumination shown in Figure 5A, the ZnO NRA and ZnO@TiO_2 NRA electrode exhibit very low photocurrent, whereas the photocurrents of the samples loaded with sulfide are obviously enhanced within the entire scanning region. The photocurrent density gradually increases with the increment of sulfide loading amount, because $ZnIn_{0.25}Cu_{0.02}S_{1.395}$ solid-solution is a visible light absorber and the more sulfide can convert the more visible light into current. At an applied potential of 0 V

versus Ag/AgCl, the current density of ZnO NRA and ZnO@TiO_2 NRA are −0.32 and −0.37 mA/cm^2, respectively. Under the same conditions, the current densities of the ZICS-1unit, ZICS-2unit, ZICS-5unit, ZICS-10unit, ZICS-15unit and ZICS-20unit are −1.27, −2.89, −4.21, −5.56, −7.39, and −5.23 mA/cm^2, respectively. Moreover, the onset potentials of the ZnO NRA and ZnO@TiO_2 NRA films are around −0.25 and −0.27 V, and the value shifts from −0.33 to −0.56 V after $ZnIn_{0.25}Cu_{0.02}S_{1.395}$ solid-solution is loaded. The negative shift of the onset potential indicates the decreased surface state densities of the electrodes and increased charge transfer rates at the interfaces.[44, 45]

The visible light responses of the samples with a UV light cut-off filter (λ > 400 nm) at an applied potential of 0 V versus Ag/AgCl are shown in Figure 5B. A higher photocurrent corresponds to a higher efficiency of hydrogen evolution of the PEC device. When the light turns on, the photocurrent reaches a peak value and gradually decays to a steady state. A longer decay time associates with a longer lifetime of photogenerated charge carriers.[46] The current densities of the ZnO NRA and ZnO@TiO_2 NRA electrodes are 0.31 and 0.34 mA/cm^2, respectively. The current densities of the ZnO@TiO_2 NRA with $ZnIn_{0.25}Cu_{0.02}S_{1.395}$ solid-solution increase from 1.25 to 7.28 mA/cm^2, which are increased about from 4 to 24 times than that of ZnO NRA sample. However, the ZnO NRA corrosion of the ZICS-20unit sample causes the decline of the photoelectrochemical performance compared with the other samples as mentioned above.

To quantify the photoelectrochemical response of the samples to incident light

with various wavelengths, the IPCE measurements were performed on the sample electrodes at 0 V versus Ag/AgCl (Figure 5C). The photoresponse of the ZnO NRA and ZnO@TiO_2 NRA are only active in the UV region. With the $ZnIn_{0.25}Cu_{0.02}S_{1.395}$ solid-solution loaded onto the ZnO@TiO_2 NRA, the photoresponse of the sample electrodes extends to the wavelength at 580 nm, which agrees with the absorption edge of $ZnIn_{0.25}Cu_{0.02}S_{1.395}$ solid-solution (Figure 3). With the increased polymetallic sulphide amount the series of ZICS samples exhibit both the extended coverage of photoresponse and the increased IPCE values in the visible light region. The ZICS-15unit electrode exhibits a maximum IPCE of approximately 43.2% at 380 nm, and then 31.8% at 420 nm, 29.3% at 440 nm, 26.2% at 460 nm and 20.5% at 480 nm, respectively. The improvement is mainly attributed to the PN heterojunctions formed between the co-axial ZnO@TiO_2 nanorod and polymetallic sulphide solid-solution on its surfaces. The ZnS nanoparticles in ZICS-20unit sample cause the photoresponse drop dramatically due to the damage of interface contact from the corrosion. In addition, we believe that the lower IPCE in the visible light region compared to the UV light region is due to mismatched band alignments of the ZnO@TiO_2 nanorod and $ZnIn_{0.25}Cu_{0.02}S_{1.395}$ solid-solution to some extent.

Electrochemical impedance spectroscopy (EIS, which are Nyquist plots here) was carried out to interpret the photocurrent change and the photon conversion efficiency of the samples. Figure 5D shows electrochemical impedance spectra of nanorod arrays at AC frequency from 100 kHz to 1 Hz, which was performed under simulated solar illumination at open circuit voltage. Considering the molecular

polarization caused by high frequency alternating-electric field, the charge transfer resistance (R_{ct}) from the photoelectrodes to redox species in the electrolyte can be calculated by fitting the semi-arc in the low frequency region. A smaller circle radius represents lower electron transport resistance and higher separation efficiency of the photogenerated electrons and holes. From Figure 5D, we can deduce that the R_{ct} of loaded $ZnIn_{0.25}Cu_{0.02}S_{1.395}$ solid-solution film is smaller than that of ZnO NRA and ZnO@TiO_2 NRA films, which explains the better photoresponse in Figure 5B. It indicates that the formed PN heterojunctions between $ZnIn_{0.25}Cu_{0.02}S_{1.395}$ solid-solution and ZnO@TiO_2 NRA establish an internal electrostatic field to promote the transportation of charge carriers and restrain the recombination of electrons and holes, so more charge carriers take part in the redox reactions. Again, the corrosion of the ZICS-20unit sample passivates the electron transmission in ZnO single-crystal by appearance of ZnS nanoparticles. Thus, its R_{ct} becomes larger than that of ZnO NRA and ZnO@TiO_2 NRA samples.

Photocatalysis and hydrogen production

Scheme 2 illustrates the photoinduced electron separation and transportation process in the ZnO@TiO_2 NRA loaded $ZnIn_{0.25}Cu_{0.02}S_{1.395}$ solid-solution. ZnO nanorods play the role as an effective percolation pathway for the transportation of electrons from $ZnIn_{0.25}Cu_{0.02}S_{1.395}$ solid-solution to inner nanorods. TiO_2, as an activated layer, has high surface-to-volume ratio for more photocatalysis reactive sites, and enhances the photocatalysis activity by exposing active (001) plane and protect ZnO from harsh environments. The coarse surface of ZnO@TiO_2 nanorod reduces the

reflection of incident light so as to increase the harvesting of incident light. $ZnIn_{0.25}Cu_{0.02}S_{1.395}$ solid-solution with direct narrow band gap and high absorption coefficiency can be employed as the visible light absorber to generate photoinduced charge carriers.

Under UV-Vis light illumination, photogenerated electrons in the conduction band of sulphide flow to that of ZnO and TiO_2, and further to the counter electrode through the external circuit to produce hydrogen. A stepwise conduction band edge limits the electrons flux and reduces the recombination of the electrons and the holes, leading to the enhancement in the photovoltaic performance. Then it significantly enhances photocurrent density and conversion efficiency of material. Furthermore, we also used the ZICS-15unit film sample for hydrogen production, and we received about 12 μmol hydrogen gas during 4 h reaction (Figure 6). Although the hydrogen gas produced within this sample system is much lower than that produced within the traditional mesoporous powder materials (e.g. commercial TiO_2 P25 powder), it is still an acceptable result considering the lower amount of uncontrollable stoichiometric loaded material due to nanorod array film in liquid reaction condition. Simultaneously, photogenerated holes in the valence band of the ZnO and TiO_2 are transferred to sulphide, which reacts with the hole scavengers S^{2-} and SO_3^{2-} adhering to the sulphide surface.

A uniform semiconductor core/layer nanostructure with effective heterojunction like this combines the merits of all components and meets the requirements of the large light absorption, the rapid separation of charge carriers and the reduction of the

surface defects of nanorods. In addition, a nanorod array film also has higher surface areas and suitable integration into micro-nanoelectronic systems.

Conclusions

A ZnO@TiO_2 core/layer nanorod arrays sensitized with the $ZnIn_{0.25}Cu_{0.02}S_{1.395}$ solid-solution nanoparticles was fabricated via a facile hydrothermal process. The photocurrent of the heteronanostructure reached to 7.28 mA/cm^2, and its IPCE was significantly enhanced in the visible light region. In such a combined nanostructure, ZnO acts as a framework and pathway for electron transport and $ZnIn_{0.25}Cu_{0.02}S_{1.395}$ solid-solution can capture a large proportion of visible light due to its high absorption coefficient and a narrow direct bandgap. TiO_2 plays the role as a protection layer to ZnO and enlarges the surface area of photocatalysis. Moreover, the ZnO nanorod with TiO_2 layer wrapped outside and the polymetallic sulphide solid-solution decorated onto surfaces together form an intimate PN heterostructure between interfaces, which accelerates charge injection from one semiconductor to another. It leads to efficient photoexcited charge separation and reduction of the recombination of electron-hole pairs by the internal electrostatic field in the interface. The above factors are supposed to be the main reasons for the enhanced photoelectrical response of our material system. We also demonstrate its great potential as the integrated photoelectric devices and solar photocatalysis water splitting.

Experimental Section

Preparation of ultralong ZnO nanorod array

To get ultralong ZnO nanorod arrays, we used polyethyleneimine (PEI) to suppress the homogeneous nucleation during the ZnO nanorod growth process. Then the polymer chain of PEI preferentially adsorbs to certain crystal faces of ZnO clusters, which initially formed due to thermal fluctuation and are small, and inhibit further crystal growth along these faces to develop the ZnO bulk. As a result, growth of ZnO nanorods can normally occur on the seeded substrates at a reasonably high growth rate.

In a typical modified route,[47, 48] the zinc acetate dehydrate and ethanolamine are mixed in a 1:1.2 mole ratio in 25 mL 2-Methoxyethanol to ensure the concentration of $Zn(CH_3COO)_2$ as 0.2 mol/L. The above solution is stirred at 60 ℃ for 30 min., and then spin-coated (3000 rpm for 1 min) on FTO glass substrates, which are ultrasonically cleaned by acetone, ethanol and deionized water in this order. Next, we put the pretreated FTO glass substrates in an electric oven at 400 ℃ for 2 h to get ZnO grains.

To prepare the ZnO nanorod array growth solution, zinc nitrate hexahydrate and hexamethylenetetramine (HMTA) are digested in 100 mL deionized water to maintain the concentration of $Zn(NO_3)_2$ as 25 mmol/L and the molar ratio of $Zn(NO_3)_2$: HMTA as 1:1. The concentration of PEI is set as 0.005 mol/L in our work. A ZnO nanorod array is grown on the FTO substrate with ZnO grains by soaking in the above solution at 90 ℃ for 12 h. Then we change with fresh growth solution to repeat the

above procedures five times to obtain ultralong nanorod arrays, and the total actual growth time should be more than 60 h in our experiments.

Preparation of ZnO@TiO_2 core/layer nanorod array film

The FTO substrate with ZnO nanorod film is put into a Teflon lined stainless steel autoclave, which contains 7.5 μL diethylenetriamine (DETA), 10.5 mL isopropyl alcohol (AR grade, Beijing Chemical Works) and 50～70 μL titanium (IV) isopropoxide. The sealed autoclave is heated up to 180 ℃ for 12 h in an electric oven. Following that, the reaction autoclave is naturally cooled down to room temperature. The as-prepared samples are gently rinsed with ethanol and acetone and dried at room temperature. Finally, the samples are annealed at 400 ℃ for 2 h to reinforce the crystal phase of TiO_2.

Preparation of ZnO@TiO_2 film loaded with Zn-In-Cu-S solid-solution

The Zn-In-Cu-S solid-solution is loaded via the solvothermal method. In a typical experiment, $Zn(CH_3COO)_2$•$2H_2O$ (0.03 mmol), $InCl_3$•$4H_2O$ (0.005 mmol), and thiourea (0.0385 mmol) were dissolved into 8 mL of ethylene glycol using a magnetic stirrer to form a clear solution. We also prepared 0.2 mL of 0.005 mol/L $Cu(CH_3COO)_2$•H_2O/ ethylene glycol solution to add dropwise into the above solution under constant stirring. The above amount and concentration of the reaction mixture can be defined as unit dose (named as ZICS-1unit), and we increase the stoichiometry according to ZICS-1unit to obtain ZICS-2unit (twice), ZICS-5unit (five times) and so on, which are named as mentioned above. The as-prepared solution is immediately transferred into an autoclave (Teflon cups with 15 mL inner volume), and the FTO

substrate with a $ZnO@TiO_2$ nanorod array film is maintained in the Teflon cup at 180 ℃ for 2 h and then air-cooled to room temperature. The FTO substrate is washed several times with absolute ethanol and finally air dried.

Material morphology and characterization

Morphology and elemental chemical composition analyses of the nanoarray photoelectrode are carried out using field emission scanning electron microscope (FESEM) JEOL JSM 4800F combined with energy-dispersive X-ray spectroscopy (EDX). The crystallographic and detailed microscopic structure analyses are observed by high resolution transmission electron microscopy (HRTEM) on FEI Tecnai F20 operated at 200 kV, equipped with a line scan profile of EDX and elemental mappings. X-ray diffraction (XRD) patterns are recorded on a Rigaku D/Max-2000 diffractometer with Cu Kα radiation (λ = 0.15406 nm). UV-Vis spectra to analyze the band gap structure are measured by a Shimadzu UV-3600 UV-Vis-NIR scanning spectrophotometer using $BaSO_4$ as a reference. A Hitachi F7000 UV-Vis spectrophotometer equipped with a Xe lamp source is employed to determine the photoluminescence spectra of our samples under different excitations.

Photoelectrochemical measurements

In our experiments, a three-electrode configuration in a quartz cell is assembled to test the photoelectrochemical activity of the samples on a Chenghua electrochemical workstation (CHI660C, Shanghai). A Pt plate and a commercially available Ag/AgCl electrode are used as the counter and reference electrodes, and the prepared samples are employed as working electrodes. The effective surface area of

the working electrode is 0.5 × 0.5 cm^2. All measured potential values are against a Ag/AgCl reference electrode unless otherwise indicated. The electrolyte used in all measurements is an aqueous solution containing 0.5 mol/L Na_2SO_4. A 300 W xenon lamp (PLS-SXE300/300UV) equipped with a UV-light cut-off filter (λ > 400 nm) is used as visible light irradiation source, and its light intensity is 100 mW/cm^2. The linear sweep voltammograms (LSV) are operated at 100 mV/s in a potential range from −0.8 V to +0.8 V versus Ag/AgCl both in dark and under illumination. The chronoamperometry curves (*I-T* curve) of the films are obtained at 0 V versus Ag/AgCl. Electrochemical impedance spectroscopy (EIS) is performed under illumination with an AC amplitude of 5 mV and frequency range between 100 kHz and 1 Hz. The PLS-SXE300/300UV xenon lamp and a monochromator (Monochromator 300, Changtuo Technology Co., Ltd.) are used to measure wavelength-dependent photocurrents of all samples. The monochromatic light intensity is measured with a radiometer for next calculations. The incident photon to electron conversion efficiency (IPCE) of the samples is calculated as follows:

$$IPCE = 1240I(\text{mA/cm}^2)/[\lambda(\text{nm})J_{\text{light}}\ (\text{mW/cm}^2)]$$

where I is the photocurrent density, λ is the wavelength of the monochromatic light, and J_{light} is the monochromatic light intensity.

Photocatalytic hydrogen production

The production is performed in a closed gas-circulation photoelectrochemical system with a side window, and we use one S15 sample in 350 mL stirring aqueous solution containing 1.0 mol/L Na_2SO_3 and 1.0 mol/L Na_2S as electron donors for

hydrogen production. The reaction without Pt material catalysis is carried out for 4 h by irradiating the mixture light from a 300 W Xe lamp, which is equipped with an optical filter (λ > 400 nm) to cut off the light in the UV region. The amount of produced hydrogen gas was measured by gas chromatography (Agilent 6820) with a thermal conductivity detector (TCD) and argon as the carrier gas.

Conflict of Interest

The authors declare no competing financial interest.

Acknowledgements

This work is supported by the National Natural Science Foundation of China (No. 61306081 and 61176016), National Basic Research Program of China (No. 2013CB933900 and 2014CB931800), Science and Technology Department of Jilin Province (No. 20130522142JH, 20121801) and Science and Technology Department of Suzhou City (No. ZXY201434). We thank the support of the "Hundred Talent Program" of CAS.

References and Notes

1. A. Fujishima and K. Honda "Electrochemical photolysis of water at a semiconductor electrode" *Nature* 1972, 238, 37-38.
2. Arthur J. Nozik and John R. Miller "Introduction to Solar Photon Conversion" *Chem. Rev.* 2010, 110, 6443-6445.
3. Timothy R. Cook, Dilek K. Dogutan, Steven Y. Reece, Yogesh Surendranath, Thomas S. Teets, and Daniel G. Nocera "Solar Energy Supply and Storage for the Legacy and Nonlegacy Worlds" *Chem. Rev.* 2010, 110, 6474-6502.
4. Anna Kubacka, Marcos Fernandez-Garcia, and Gerardo Colon "Advanced Nanoarchitectures for Solar Photocatalytic Applications" *Chem. Rev.* 2012, 112, 1555-1614.
5. Nathan S. Lewis and Daniel G. Nocera "Powering the planet: Chemical challenges in solar energy utilization" *Proc. Natl. Acad. Sci. U.S.A.* 2006, 103, 15729-15735.
6. James Barber "Biological solar energy" *Phil. Trans. R. Soc. A* 2007, 365, 1007-1023.
7. Yen-Hsun Su, Yuan-Feng Ke, Shi-Liang Cai1 and Qian-Yu Yao "Surface plasmon resonance of layer-by-layer gold nanoparticles induced photoelectric current in environmentally-friendly plasmon-sensitized solar cell" *Light: Science & Applications* 2012, 1, e14; doi:10.1038/lsa.2012.14.
8. Emily D Kosten, Jackson H Atwater, James Parsons, Albert Polman and Harry A Atwater "Highly efficient GaAs solar cells by limiting light emission angle" *Light:*

Science & Applications 2013, 2, e45; doi:10.1038/lsa.2013.1.

9. Allen J. Bard and Marye Anne Fox "Artificial Photosynthesis: Solar Splitting of Water to Hydrogen and Oxygen" *Acc. Chem. Res*. 1995, 28, 141-145.
10. Yasuhiro Tachibana, Lionel Vayssieres and James R. Durrant "Artificial photosynthesis for solar water-splitting" *Nat. Photonics* 2012, 6, 511-518.
11. Rufino M. Navarro, M. Consuelo Alvarez-Galvan, Jose A. Villoria de la Mano, Saeed M. Al-Zahrani and Jose Luis G. Fierro "A framework for visible-light water splitting" *Energy Environ. Sci.* 2010, 3, 1865-1882.
12. Frank E. Osterloh "Inorganic nanostructures for photoelectrochemical and photocatalytic water splitting" *Chem. Soc. Rev.* 2013,42, 2294-2320.
13. Xiaobo Chen, Lei Liu, Peter Y. Yu, and Samuel S. Mao "Increasing Solar Absorption for Photocatalysis with Black Hydrogenated Titanium Dioxide Nanocrystals" *Science* 2011, 331, 746-750.
14. M. Murdoch, G. I. N. Waterhouse, M. A. Nadeem, J. B. Metson, M. A. Keane, R. F. Howe, J. Llorca and H. Idriss "The effect of gold loading and particle size on photocatalytic hydrogen production from ethanol over Au/TiO_2 nanoparticles" *Nat. Chem.* 2011, 3, 489-492.
15. Gongming Wang, Hanyu Wang, Yichuan Ling, Yuechao Tang, Xunyu Yang, Robert C. Fitzmorris, Changchun Wang, Jin Z. Zhang, and Yat Li "Hydrogen-Treated TiO_2 Nanowire Arrays for Photoelectrochemical Water Splitting" *Nano Lett.* 2011, 11, 3026-3033.
16. Charles Y. Cummings, Frank Marken, Laurence M. Peter, K. G. Upul Wijayantha,

and Asif A. Tahir "New Insights into Water Splitting at Mesoporous α-Fe_2O_3 Films: A Study by Modulated Transmittance and Impedance Spectroscopies" *J. Am. Chem. Soc.* 2012, 134, 1228-1234.

17. Benjamin Klahr, Sixto Gimenez, Francisco Fabregat-Santiago, Juan Bisquert, and Thomas W. Hamann "Photoelectrochemical and Impedance Spectroscopic Investigation of Water Oxidation with "Co–Pi"-Coated Hematite Electrodes" *J. Am. Chem. Soc.* 2012, 134, 16693-16700.
18. Akihiko Kudo and Yugo Miseki "Heterogeneous photocatalyst materials for water splitting" *Chem. Soc. Rev.*, 2009, 38, 253-278.
19. C. Klingshirn "ZnO: Material, Physics and Applications" *Chem. Phys. Chem.*, 2007, 8, 782-803.
20. Yang Bai, Hua Yu, Zhen Li, Rose Amal, Gao Qing (Max) Lu, and Lianzhou Wang "In Situ Growth of a ZnO Nanowire Network within a TiO_2 Nanoparticle Film for Enhanced Dye-Sensitized Solar Cell Performance" *Adv. Mater.*, 2012, DOI: 10.1002/adma.201201992.
21. Sheng Chu, Guoping Wang, Weihang Zhou, Yuqing Lin, Leonid Chernyak, Jianze Zhao, Jieying Kong, Lin Li, Jingjian Ren and Jianlin Liu "Electrically pumped waveguide lasing from ZnO nanowires" *Nat. Nanotechnol.*, 2011, 8, 506-510.
22. Hua Gui Yang, Gang Liu, Shi Zhang Qiao, Cheng Hua Sun, Yong Gang Jin, Sean Campbell Smith, Jin Zou, Hui Ming Cheng, and Gao Qing (Max) Lu "Solvothermal Synthesis and Photoreactivity of Anatase TiO_2 Nanosheets with Dominant {001} Facets" *J. Am. Chem. Soc.* 2009, 131, 4078-4083.

23. Yunqian Dai, Claire M. Cobley, Jie Zeng, Yueming Sun, and Younan Xia "Synthesis of Anatase TiO_2 Nanocrystals with Exposed {001} Facets" *Nano Lett.* 2009, 9, 2455-2459.

24. Wen Qi Fang, Xue-Qing Gong, and Hua Gui Yang "On the Unusual Properties of Anatase TiO_2 Exposed by Highly Reactive Facets" *J. Phys. Chem. Lett.* 2011, 2, 725-734.

25. Shrabani Panigrahi and Durga Basak "Core-shell TiO_2@ZnO nanorods for efficient ultraviolet photodetection" *Nanoscale* 2011, 3, 2336-2341.

26. Xiaodong Yan, Chongwen Zou, Xiangdong Gao and Wei Gao "ZnO/TiO_2 core-brush nanostructure: processing, microstructure and enhanced photocatalytic activity" *J. Mater. Chem.* 2012, 22, 5629-5640.

27. S. Girish Kumar and L. Gomathi Devi "Review on Modified TiO_2 Photocatalysis under UV/Visible Light: Selected Results and Related Mechanisms on Interfacial Charge Carrier Transfer Dynamics" *J. Phys. Chem. A* 2011, 115, 13211-13241.

28. Yu-Xiang Yu, Wei-Xin Ouyang, Zhou-Ting Liao, Bin-Bin Du, and Wei-De Zhang "Construction of ZnO/ZnS/CdS/$CuInS_2$ Core-Shell Nanowire Arrays via Ion Exchange: p-n Junction Photoanode with Enhanced Photoelectrochemical Activity under Visible Light" *ACS Appl. Mater. Interfaces* 2014, 6, 8467-8474.

29. Jun Xu, Xia Yang, Hongkang Wang, Xue Chen, Chunyan Luan, Zongxiang Xu, Zhenzhen Lu, V. A. L. Roy, Wenjun Zhang, and Chun-Sing Lee "Arrays of ZnO/$Zn_xCd_{1-x}Se$ Nanocables: Band Gap Engineering and Photovoltaic Applications" *Nano Lett.* 2011, 11, 4138-4143.

30. Wenjun Sheng, Bo Sun, Tielin Shi, Xianhua Tan, Zhengchun Peng, and Guanglan Liao "Quantum Dot-Sensitized Hierarchical Micro/Nanowire Architecture for Photoelectrochemical Water Splitting" *ACS Nano* 2014, 8, 7163-7169.

31. Minsu Seol, Easwaramoorthi Ramasamy, Jinwoo Lee, and Kijung Yong "Highly Efficient and Durable Quantum Dot Sensitized ZnO Nanowire Solar Cell Using Noble-Metal-Free Counter Electrode" *J. Phys. Chem. C* 2011, 115, 22018-22024.

32. Jun Xu, Chun-Yan Luan, Yong-Bing Tang, Xue Chen, Juan Antnio Zapien, Wen-Jun Zhang, Hoi-Lun Kwong, Xiang-Min Meng, Shuit-Tong Lee, and Chun-Sing Lee "Low-Temperature Synthesis of $CuInSe_2$ Nanotube Array on Conducting Glass Substrates for Solar Cell Application" *ACS Nano* 2010, 4, 6064-6070.

33. Joel Jean, Sehoon Chang, Patrick R. Brown, Jayce J. Cheng, Paul H. Rekemeyer, Moungi G. Bawendi, Silvija Gradecak2 and Vladimir Bulovic "ZnO Nanowire Arrays for Enhanced Photocurrent in PbS Quantum Dot Solar Cells" *Adv. Mater.* 2013, 25, 2790-2796.

34. Jianbo Gao, Joseph M. Luther, Octavi E. Semonin, Randy J. Ellingson, Arthur J. Nozik, and Matthew C. Beard "Quantum Dot Size Dependent *J-V* Characteristics in Heterojunction ZnO/PbS Quantum Dot Solar Cells" *Nano Lett.* 2011, 11, 1002-1008.

35. Benjamin D. Yuhas and Peidong Yang "Nanowire-Based All-Oxide Solar Cells" *J. Am. Chem. Soc.* 2009, 131, 3756-3761.

36. Hiroaki Tada, Tomohiro Mitsui, Tomokazu Kiyonaga, Tomoki Akita and Koji

Tanaka "All-solid-state Z-scheme in CdS-Au-TiO_2 three-component nanojunction system" *Nat. Mater.* 2006, 5, 782-786.

37. Da Chen, Hao Zhang, Song Hu, and Jinghong Li "Preparation and Enhanced Photoelectrochemical Performance of Coupled Bicomponent ZnO-TiO_2 Nanocomposites" *J. Phys. Chem. C* 2008, 112, 117-122.
38. A. J. Nozik, M. C. Beard, J. M. Luther, M. Law, R. J. Ellingson, and J. C. Johnson "Semiconductor Quantum Dots and Quantum Dot Arrays and Applications of Multiple Exciton Generation to Third-Generation Photovoltaic Solar Cells" *Chem. Rev.* 2010, 110, 6873-6890.
39. Lei Ge, Fan Zuo, Jikai Liu, Quan Ma, Chen Wang, Dezheng Sun, Ludwig Bartels, and Pingyun Feng "Synthesis and Efficient Visible Light Photocatalytic Hydrogen Evolution of Polymeric g-C_3N_4 Coupled with CdS Quantum Dots" *J. Phys. Chem. C* 2012, 116, 13708-13714.
40. Andreas Menzel, Kittitat Subannajui, Firat Güder, Dominik Moser, Oliver Paul, and Margit Zacharias "Multifunctional ZnO-Nanowire-Based Sensor" *Adv. Funct. Mater.* 2011, 21, 4342-4348.
41. Siou-Yi Lin, Shoou-Jinn Chang, and Ting-Jen Hsueh "ZnO nanowires modified with Au nanoparticles for nonenzymatic amperometric sensing of glucose" *Appl. Phys. Lett.* 2014, 104, 193704-1-5.
42. Ruomeng Yu, Caofeng Pan, and Zhong Lin Wang "High performance of ZnO nanowire protein sensors enhanced by the piezotronic effect" *Energy Environ. Sci.* 2013, 6, 494-499.

43. Yingxuan Li, Gang Chen, Qun Wang, Xu Wang, Ankun Zhou, and Zaoyu Shen "Hierarchical ZnS-In_2S_3-CuS Nanospheres with Nanoporous Structure: Facile Synthesis, Growth Mechanism, and Excellent Photocatalytic Activity" *Adv. Funct. Mater.* 2010, 20, 3390-3398.

44. Yoon, K. H., Shin, C. W., and Kang, D. H. "Photoelectrochemical Conversion in a WO_3 Coated p-Si Photoelectrode: Effect of Annealing Temperature" *J. Appl. Phys.* 1997, 81, 7024-7029.

45. Yoon K. H., Seo D. K., Cho Y. S., and Kang D. H. "Effect of Pt Layers on the Photoelectrochemical Properties of a WO_3/p-Si Electrode" *J. Appl. Phys.* 1998, 84, 3954-3959.

46. Dai G. P., Yu J. G., and Liu, G. "Synthesis and Enhanced Visible-Light Photoelectrocatalytic Activity of p-n Junction BiOI/TiO_2 Nanotube Arrays" *J. Phys. Chem. C* 2011, 115, 7339-7346.

47. Matt Law, Lori E. Greene, Justin C. Johnson, Richard Saykally and Peidong Yang "Nanowire dye-sensitized solar cells" *Nat. Mater.* 2005, 4, 455-459.

48. Chengkun Xu, Paul Shin, Liangliang Cao, and Di Gao "Preferential Growth of Long ZnO Nanowire Array and Its Application in Dye-Sensitized Solar Cells" *J. Phys. Chem. C* 2010, 114, 125-129.

Figures and Captions (in order)

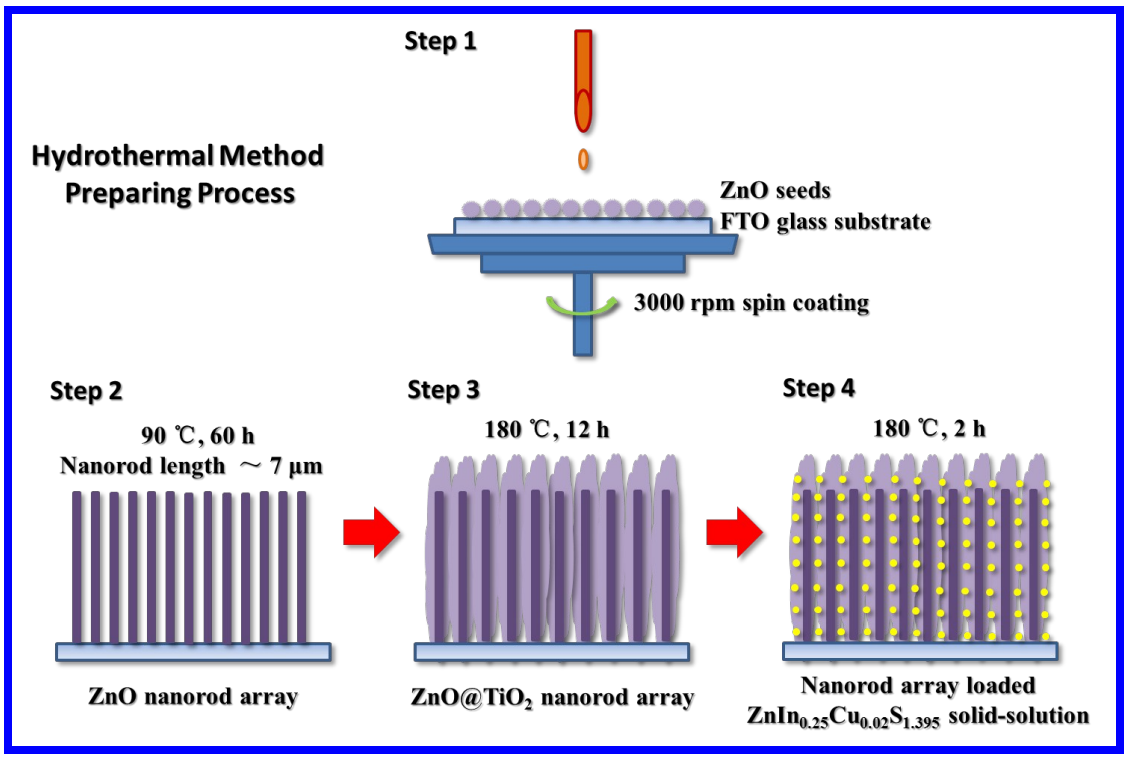

Scheme 1 Hydrothermal fabrication process of $ZnO@TiO_2$ nanorod array film loaded with polymetallic sulphide solid-solution.

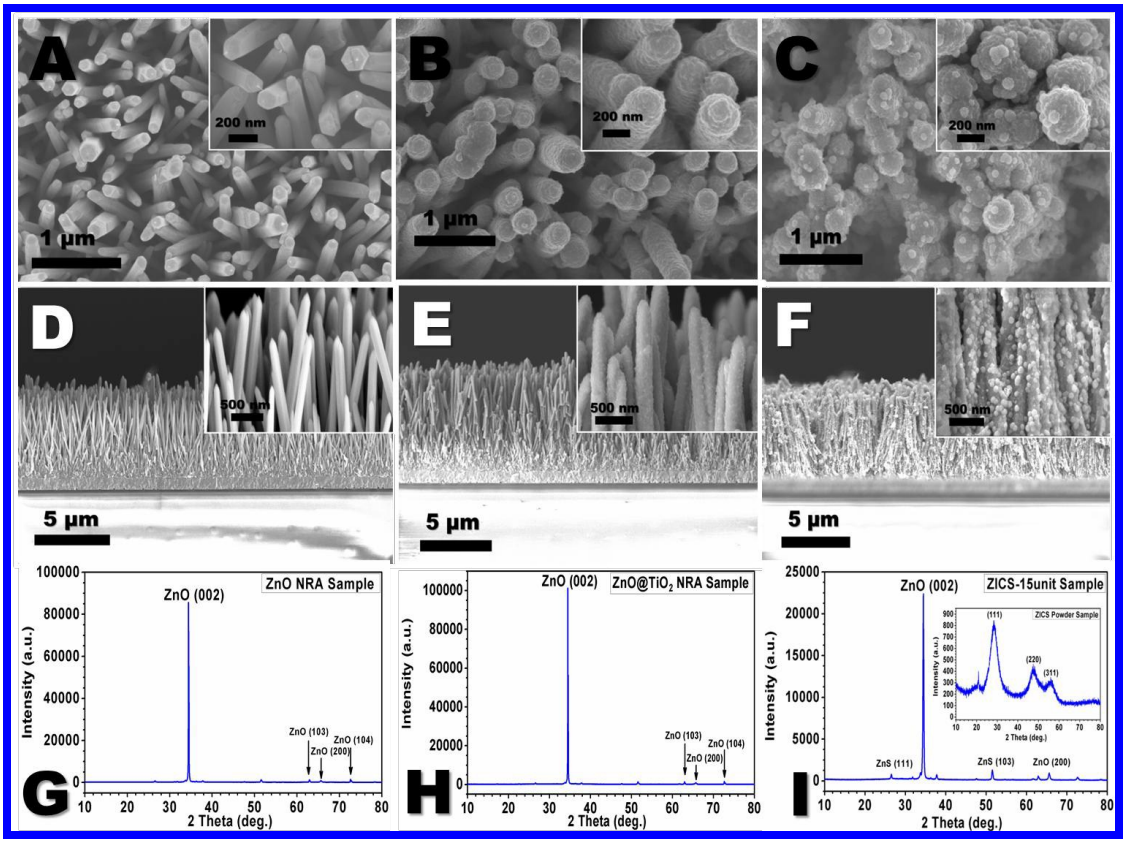

Figure 1 Field emission scanning electron microscope (FESEM) images of related samples. (A) Top-view of ZnO NRA, (B) Top-view of ZnO@TiO_2 NRA, (C) Top-view of ZICS-15unit sample, (D), (E) and (F) are the side-views corresponding to (A), (B) and (C), respectively. All the insets as shown are the corresponding magnification views. Meanwhile, the corresponding X-ray diffraction (XRD) patterns are shown as (G) ZnO NRA , (H) ZnO@TiO_2 NRA, and (I) ZICS-15unit sample. The inset of (I) is the XRD pattern of ZICS powder sample as reference.

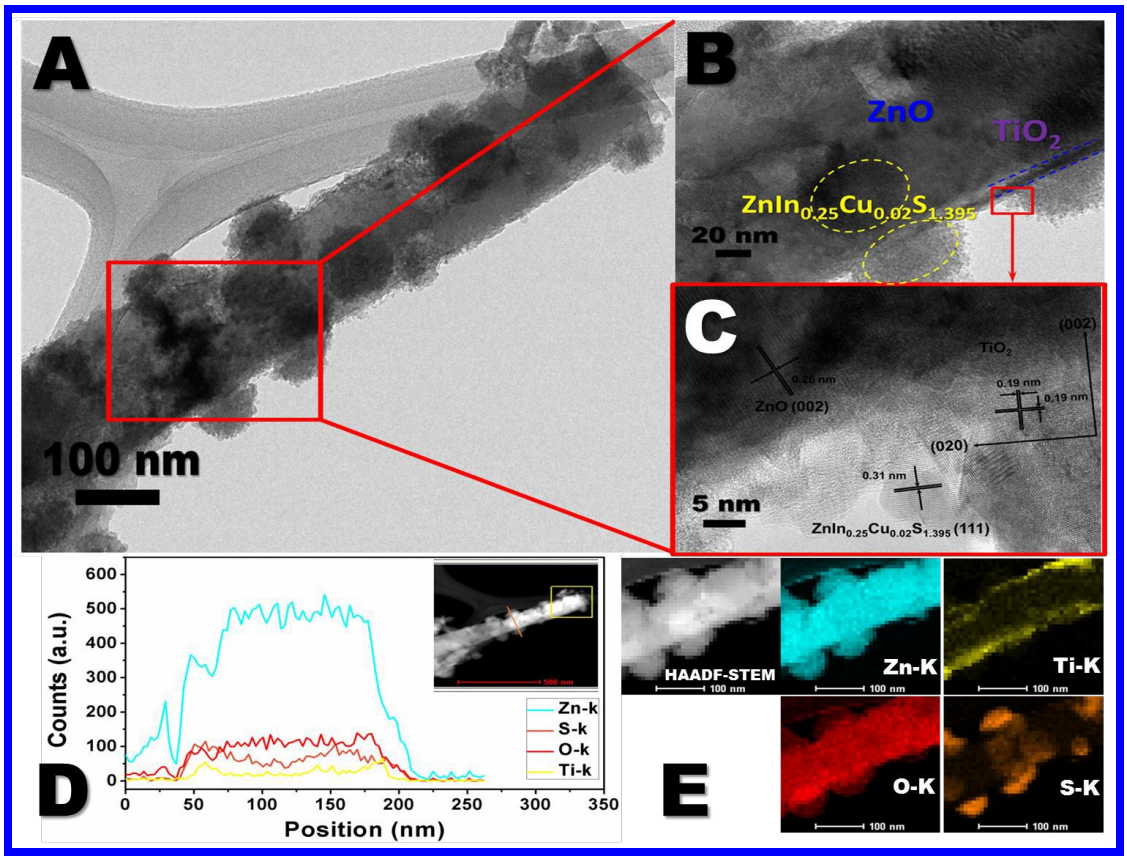

Figure 2 (A) Transmission electron microscope (TEM) image of ZICS-15unit sample, (B) and (C) High resolution TEM (HRTEM) images of the selected square area shown in (A), (D) Line scan profile of EDX spectra. It goes along the orange line crossing the nanorod as shown in the inset, which is high angle annular dark-field scanning TEM (HAADF-STEM) image. The yellow square is the reference area for image signal processing, (E) Elemental mappings of the ZICS-15unit sample.

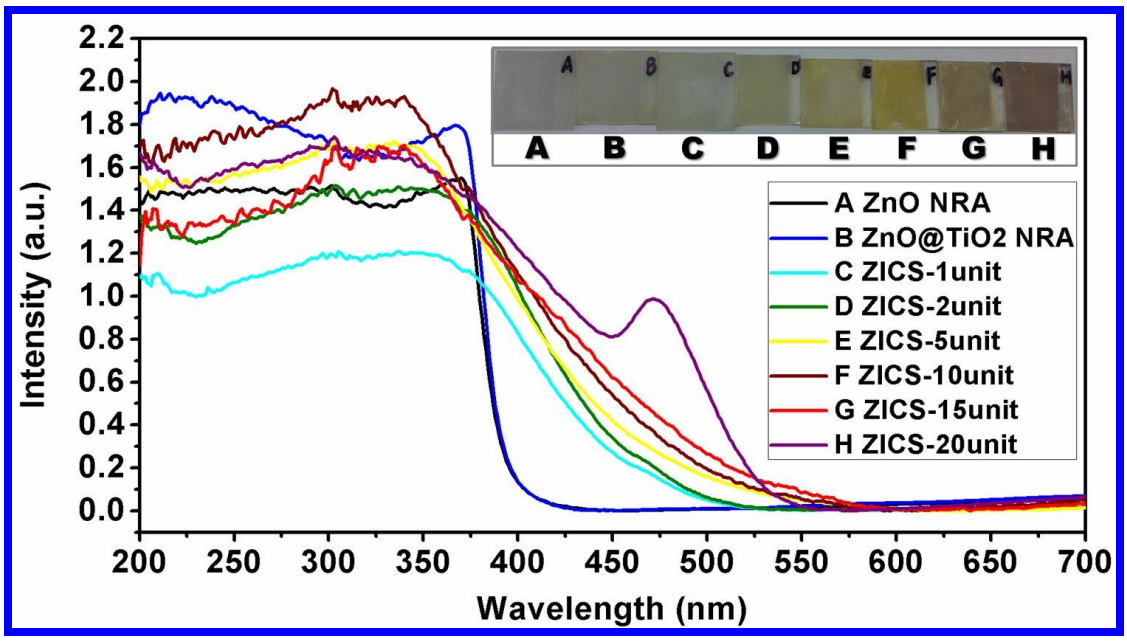

Figure 3 UV-Vis absorption spectra of nanorod array film samples mentioned in this work. Insets are the optical images of corresponding samples.

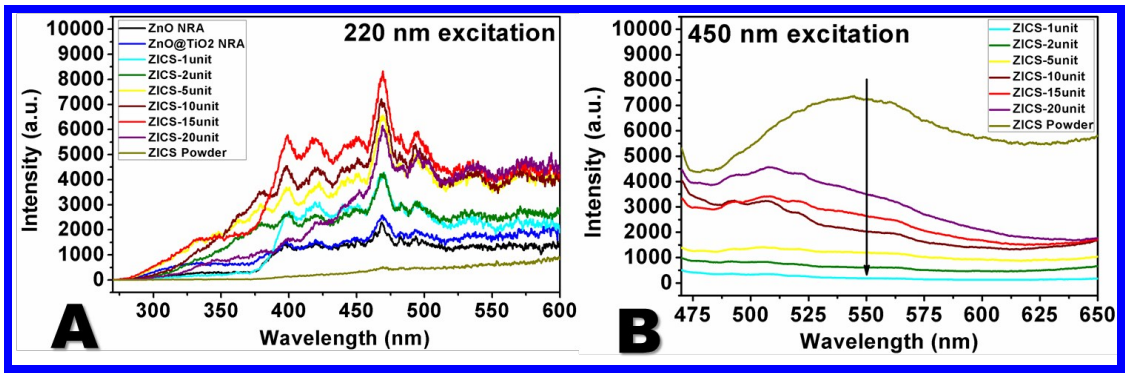

Figure 4 Photoluminescence spectra of nanorod array film samples mentioned in this work. (A) Emission spectra under 220 nm laser excitation, (B) Emission spectra under 450 nm laser excitation.

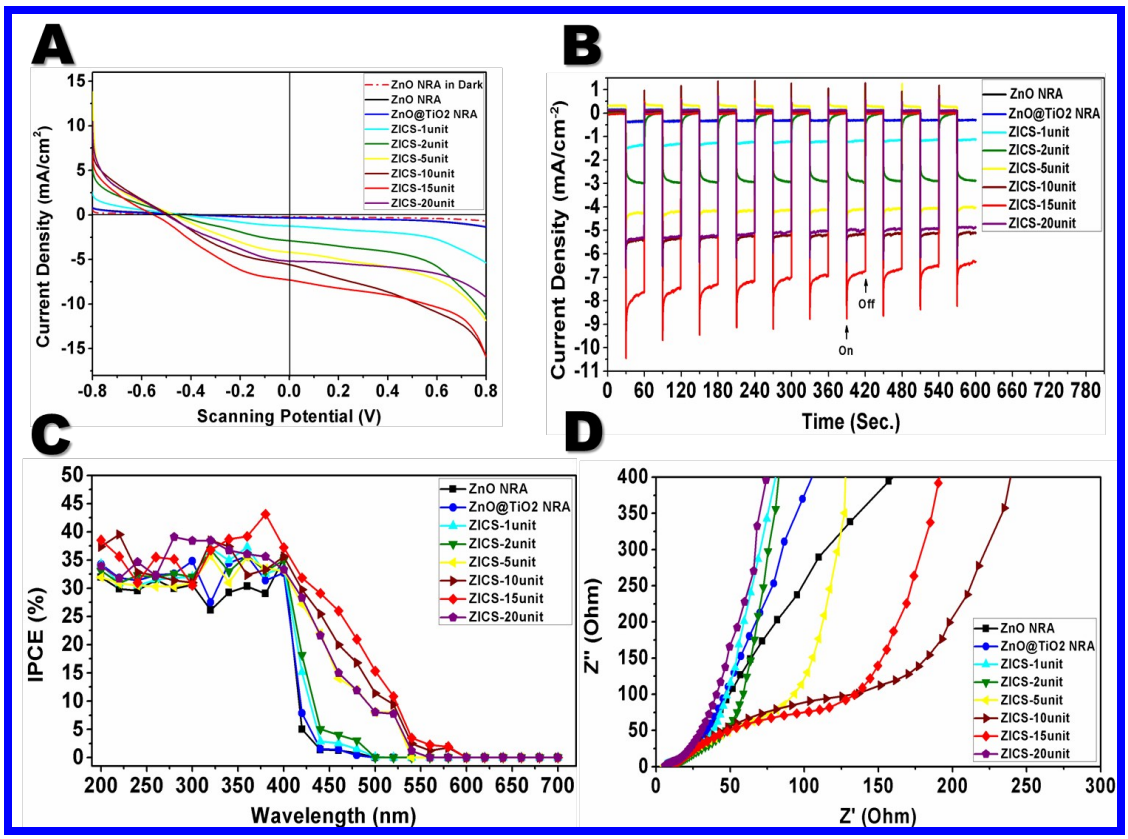

Figure 5 Photoelectrochemical measurements. (A) Current-potential curves of corresponding samples in 0.5 mol/L Na_2SO_4 solution. Scan rate: 100 mV/s, (B) *I-T* curves of corresponding samples in 0.5 mol/L Na_2SO_4 solution, applied potential 0 V versus Ag/AgCl with a UV light cut-off filter (λ > 400 nm), (C) IPCE profiles of corresponding samples collected at 0 V versus Ag/AgCl, AC amplitude: 5 mV, frequency range: 100 kHz ～ 1 Hz, (D) Electrochemical impedance spectra (EIS, Nyquist plots) of corresponding samples at 0 V versus Ag/AgCl.

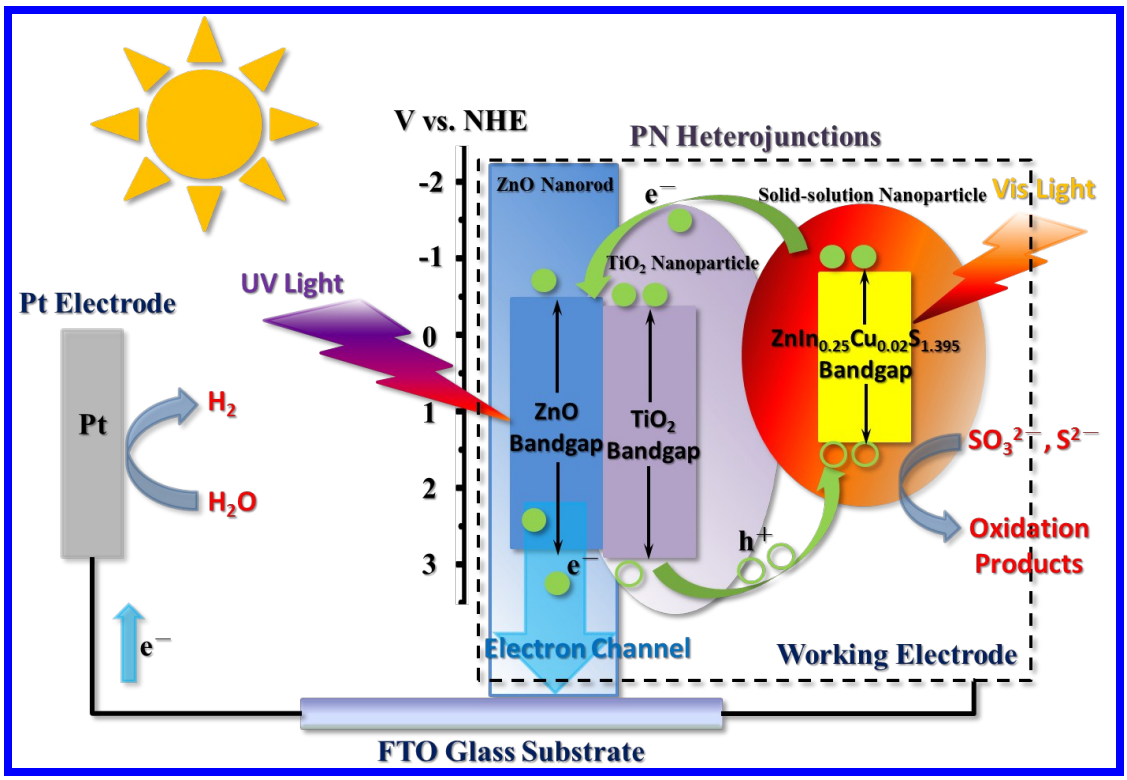

Scheme 2 Photoinduced electron separation and transportation process in the ZnO@TiO_2 nanorod array film loaded with $ZnIn_{0.25}Cu_{0.02}S_{1.395}$ solid-solution.

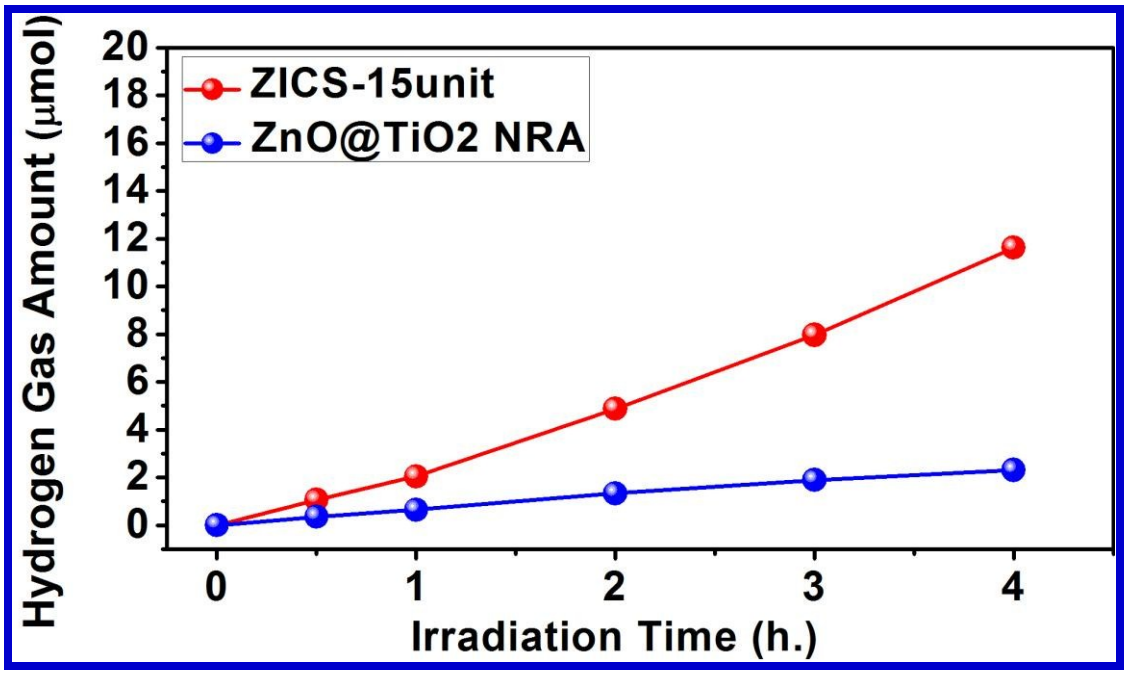

Figure 6 Amount of H_2 evolution according to reaction time for one ZICS-15unit sample and one ZnO@TiO_2 NRA sample, respectively. The 350 mL reaction vessel contains 1.0 mol/L Na_2SO_3 and 1.0 mol/L Na_2S stirring aqueous solution as electron donors.